Umbrella Meshes: Elastic Mechanisms for Freeform Shape Deployment

YINGYING REN*, EPFL, Switzerland
UDAY KUSUPATI*, EPFL, Switzerland
JULIAN PANETTA, UC Davis, USA
FLORIN ISVORANU, EPFL, Switzerland
DAVIDE PELLIS, EPFL, Switzerland
TIAN CHEN, University of Houston, USA
MARK PAULY, EPFL, Switzerland

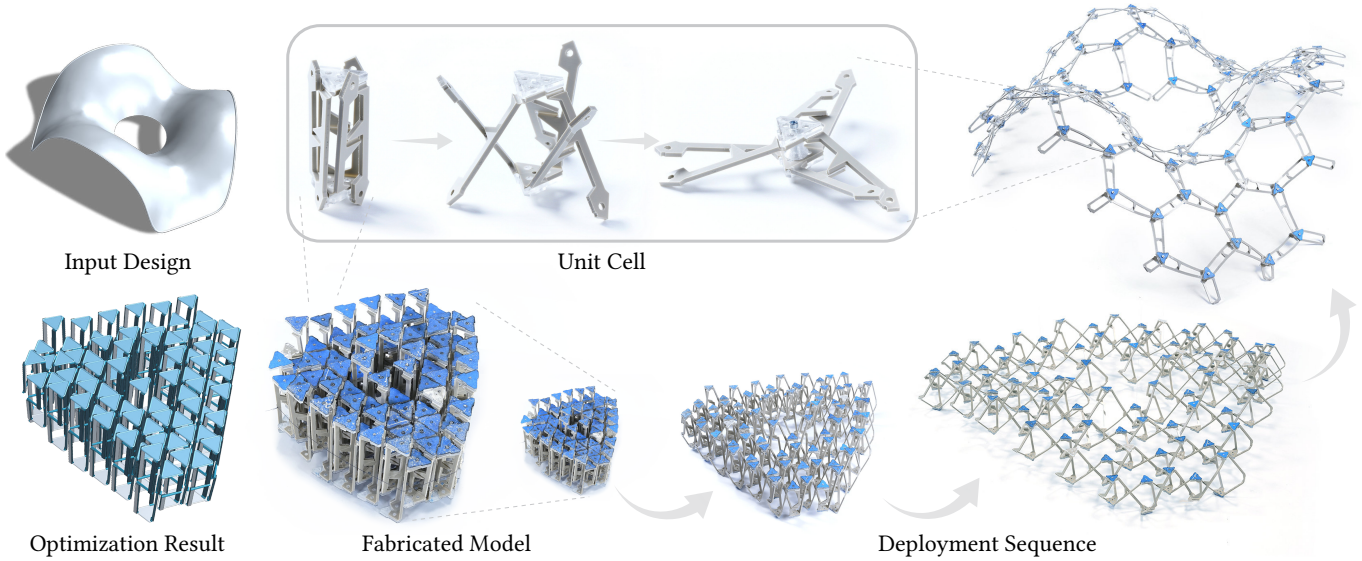

Fig. 1. An *umbrella mesh* is a volumetric deployable structure with a compact, zero-energy rest state that deploys into a given 3D target surface. We show here the physical model of an umbrella mesh unit cell and the deployment sequence of an umbrella mesh prototype optimized to match the input design surface.

We present a computational inverse design framework for a new class of volumetric deployable structures that have compact rest states and deploy into bending-active 3D target surfaces. *Umbrella meshes* consist of elastic beams, rigid plates, and hinge joints that can be directly printed or assembled in a zero-energy fabrication state. During deployment, as the elastic beams of varying heights rotate from vertical to horizontal configurations, the entire structure transforms from a compact block into a target curved surface. Umbrella Meshes encode both intrinsic and extrinsic curvature of the target surface and in principle are free from the area expansion ratio bounds of past auxetic material systems.

We build a reduced physics-based simulation framework to accurately and efficiently model the complex interaction between the elastically deforming components. To determine the mesh topology and optimal shape parameters for approximating a given target surface, we propose an inverse design optimization algorithm initialized with conformal flattening. Our algorithm minimizes the structure's strain energy in its deployed state and optimizes actuation forces so that the final deployed structure is in stable equilibrium close to the desired surface with few or no external constraints. We validate our approach by fabricating a series of physical models at various scales using different manufacturing techniques.

CCS Concepts: • **Computing methodologies** → **Shape Modeling**; **Simulation**.

Additional Key Words and Phrases: deployable structure, physics-based simulation, numerical optimization, computational design, fabrication

ACM Reference Format:
Yingying Ren*, Uday Kusupati*, Julian Panetta, Florin Isvoranu, Davide Pellis, Tian Chen, and Mark Pauly. 2022. Umbrella Meshes: Elastic Mechanisms for Freeform Shape Deployment. *ACM Trans. Graph.* 41, 4, Article 1 (July 2022), 15 pages. https://doi.org/10.1145/3528223.3530089

Authors' addresses: Y. Ren*, EPFL, yingying.ren@epfl.ch; U. Kusupati*, EPFL, uday.kusupati@epfl.ch; J. Panetta, UC Davis, julian.panetta@gmail.com; F. Isvoranu, EPFL, florin.isvoranu@epfl. ch; D. Pellis, EPFL, davide.pellis@epfl. ch; T. Chen, University of Houston, tianchen@uh.edu; M. Pauly, EPFL, mark.pauly@epfl.ch.
*joint first authors (order determined by coin toss).

0730-0301/2022/7-ART1 $15.00
https://doi.org/10.1145/3528223.3530089

1 INTRODUCTION

Deployable structures are widely used in industrial and consumer products, medical devices, aerospace applications, and civil installations [Molinari et al. 2011; Tang et al. 2017]. The ability to transform between different geometric states offers unique advantages such as compact storage and transport, simpler fabrication or assembly, and multi-functionality. Examples of deployable structures include temporary shelters, satellites, space-based solar panels [Chen et al. 2019], heart stents [Tomita et al. 2015], inflatable buildings, robotic surgical tools, and scissor lifts [Randall et al. 2012].

Rigid linkage mechanisms are one important class of deployable structures. Typically composed of rigid elements connected via rotational joints, such transformable assemblies can be modeled and optimized based on kinematic analysis [McCarthy and Soh 2010]. One iconic example is the Hoberman sphere that continuously transforms between compact and extended spherical states (Figure 2a). Compared to rigid linkage mechanisms, bending-active deployable structures have a richer shape space and offer additional functionalities. For example, deployable gridshells can assume a variety of curved shapes by allowing the individual beams to bend and twist in addition to pivoting around the connecting joints (see Figure 2b).

Within this context, we propose a new deployable material system that combines the advantages of rigid linkage mechanisms and elastic beams to enable a wide variety of freeform shapes. Our work is inspired by a classical every-day deployable object, the umbrella. Most umbrellas use a compliant linkage structure to expand a fabric to the desired covering surface when deployed. We call our structures *umbrella meshes* as they are composed of regular arrangements of parameterized cells, each consisting of an umbrella-like mechanism (Figure 3).

The key feature of umbrella meshes is that neighboring umbrella cells are *geometrically incompatible* when deployed to their expanded configurations. Although each cell covers the same area footprint in the undeployed state, the differing cell heights cause this area to expand by different amounts during deployment. Umbrella elements are thus forced to deform out-of-plane to accommodate the kinematic incompatibilities with their neighbors. Importantly, the undeployed state has no such incompatibility and so is free of residual stresses. This ensures easy assembly and enables direct fabrication with single-piece 3D printing.

Contributions. Manual design of umbrella meshes is challenging due to the complex interplay of elastically deforming elements during deployment. To address this challenge, we make several technical contributions. In particular, we present

- a generalized joint model for elastic beam structures supporting arbitrary rotation axes and positional offsets,
- a numerical algorithm to optimize the free design parameters of umbrella meshes such that the simulated equilibrium state best approximates a given target design,
- a complete inverse design pipeline that incorporates a geometric flattening algorithm to find a suitable initialization for the optimization, and
- a specific material implementation based on compliant hinge joints that simplifies fabrication and assembly.

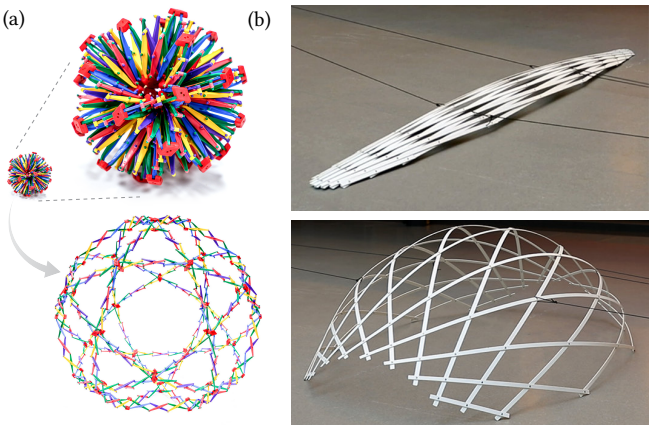

Fig. 2. The Hoberman sphere (a) is based on a rigid linkage mechanism [Hoberman 1991], while deployable elastic gridshells (b) use flexible beams that deform as the structure is deployed [Panetta et al. 2019].

We evaluate our computational framework with a number of design studies and validate the predictive accuracy of our simulations with physical prototypes. These examples demonstrate how our approach enables deployable surface geometries that are not possible with existing methods.

Our work addresses several limitations of previous deployable systems. First, umbrella meshes can undergo in principle unlimited area expansion during deployment since the rotating umbrella beams are not restricted in height. Second, in addition to controlling intrinsic curvature through metric frustration, we can also directly prescribe extrinsic curvature by introducing asymmetry in the out-of-plane dimension. Third, we can improve the stiffness of the deployed system by controlling its structural depth through partial deployment of the umbrella cells.

The full implementation code and model data for our paper are available at https://go.epfl.ch/umbrella.

2 RELATED WORK

Periodic linkages composed of identical rigid elements are commonly used to deploy simple structures such as scissor lifting platforms. With recent advances in digital fabrication technologies, spatial variation in material systems is increasingly employed for the deployment of complex bending-active structures. In particular, shape transformation from a planar state to a desired curved surface is an active research problem due to several benefits including simplified fabrication and ease of transportation. These advanced material systems require computational optimization tools to navigate the often complex design spaces that render manual design inefficient or even infeasible. We discuss below related work touching upon these aspects but also refer to the general references given in Section 1 for a broader context.

Scissor structures. Scissor mechanisms are widely-used deployable structures consisting of rigid linkages. Roovers and De Temmerman [2017] provide a comprehensive overview of translational scissor grids and discuss the design and analysis of assemblies of scissor linkages with a smooth and stress-free deployment behavior.

Zhang and colleagues [2015] propose an algorithm that generates a planar deployable scissor structure transforming between the given source and target curves in 2D. The Hoberman Sphere [Hoberman 1991] is a well-known scissor structure consisting of angulated scissor units. Roovers and co-workers [2013] present an approach to convert an arbitrary continuous surface into an angulated scissor grid using principal meshes. The compactness of these angulated scissor grids is limited by collisions of the beams.

Zheng and colleagues [2016] generate compact scissor linkages that approximate 3D target shapes. Their method optimizes for collision avoidance during folding to maximize contractibility. The main difference between these rigid scissor linkages and umbrella meshes is that we leverage geometric incompatibility and elastically deforming beams to produce bending-active structures, requiring a fundamentally different computational design approach.

Bending-active structures. Structures with elastically deforming elements have been extensively studied in the field of architecture and civil engineering. We refer to [Lienhard and Gengnagel 2018] for an overview of recent advances in bending-active structures. Below we discuss specific aspects relevant for umbrella meshes.

Bistable scissor structures are comprised of beams that are straight in the compact and deployed configurations but undergo *snap-through* buckling during deployment. Arnouts and coworkers [2018] propose a finite-element model to explore the structural response of these bistable scissor structures, particularly under self-weight. Zhang and colleagues [2021] present a computational framework to design planar compliant structures that are optimized to be stable at desired 2D poses of the structure. As we discuss in Section 6, we also observe bistable behavior in our optimized 3D umbrella meshes.

Utilizing geometric incompatibilities of variable-spacing scissor mechanisms when expanding, X-Shells [Panetta et al. 2019] and geodesic gridshells [Pillwein et al. 2020; Pillwein and Musialski 2021] allow the design of curved deployable structures through deformation of the constituting elastic rods. Contrary to these in-plane mechanisms, our umbrella meshes arrange compliant scissor mechanisms orthogonally to the surface.

Planar-to-curved deployment. To simplify fabrication, numerous material systems are deployed from a planar initial state towards a curved target state. One general computational approach is to first compute surface parameterizations whose map distortions approximately model the deformation process and then translate the parameters into spatial variations in the material systems. For auxetic material systems, the transformation between planar and curved states has been abstracted by conformal mapping [Chen et al. 2021; Konaković et al. 2016; Konaković-Luković et al. 2018]. Panetta and co-workers [2021] compute an anisotropic flattening of the target surface to a plane that complies with the metric distortion of air channel inflation. FlexMaps [Malomo et al. 2018] use an ARAP-mapping [Liu et al. 2008] to minimize distortion and optimize for a set of flat panels that curve into the desired 3D shape when assembled. Chebyshev nets are applied in [Garg et al. 2014; Sageman-Furnas et al. 2019] to model surface transformations that allow shearing but not stretching along the principal directions.

Perez and colleagues [2017] and Jourdan et al. [2020] embed elastic rods in a pre-stretched fabric. The interactions between the rods and the pre-stretch drive deployment into a curved shape. Similarly, Guseinov et al. [2017] attach rigid tiles to pre-stretched membranes to produce a composite structure that self-deploys with programmed intrinsic and extrinsic curvature. However, the non-zero stress fabrication states of all these methods inherently complicate the fabrication process.

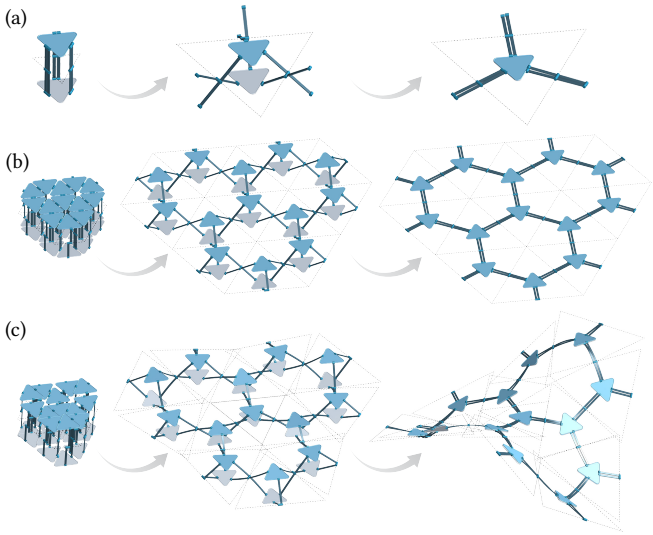

Fig. 3. Key principles of umbrella meshes. A single umbrella mechanism is deployed by pushing the two triangular plates towards each other, inducing a rotation of the vertical scissor beams into the plane (a). The triangular area footprint, sketched with dashed lines, increases during deployment. Regular tessellations of identical umbrella cells expand in plane (b). Spatially varying umbrella heights lead to incompatible deployed area footprints, and the structure buckles into a curved shape (c).

Physics-aware elastic object design. Many past works have employed shape and topology optimization to design elastic objects meeting deformation or load-bearing goals. A comprehensive review is outside the scope of our paper, and we limit our discussion to some of the most closely related research. Chen et al. [2014] use a numerical continuation method to efficiently solve for the rest shape such that a target deformed shape satisfies nonlinear static equilibrium constraints. Past work designing optimal rest shapes for balloons [Skouras et al. 2012], actuated deformable characters [Skouras et al. 2013], and fabric formwork [Zhang et al. 2019] has posed a single optimization problem over both deformation and rest shape variables that enforces static equilibrium using a set of nonlinear equality constraints. Augmented Lagrangian solvers are effective at handling the large numbers of constraints in these formulations; however, force balance constraints alone cannot distinguishing *stable* equilibria from unstable ones. Alternatively, a reduced formulation has been employed in many shape and material optimization works wherein the optimization problem is posed over only the design variables, and a nested equilibrium solver computes the stable equilibrium as a function of these design variables [Bickel et al. 2009; Panetta et al. 2021; Perez et al. 2015]. We take this approach and adopt the same first- and second-order sensitivity analysis method

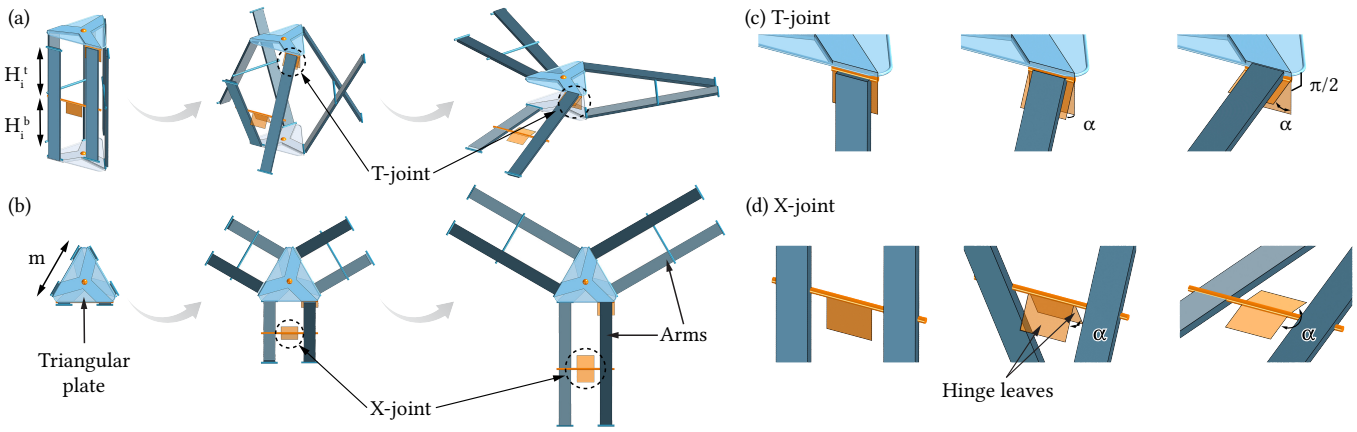

Fig. 4. Umbrella mesh joint representation. Diagrams (a) and (b) show the side and top views of the deployment of a unit cell; (c) and (d) demonstrate how our generalized joint model represents the two types of joints used in the unit.

used in [Panetta et al. 2019; Ren et al. 2021] to efficiently differentiate through the equilibrium solver with respect to the design variables. The reduced formulation has been extended to design under worst-case loading scenarios by using three levels of nested optimization [Panetta et al. 2017; Schumacher et al. 2018].

3 UMBRELLA MESH MATERIAL SYSTEM

Umbrella meshes are composed of a triangular tessellation of umbrella unit cells as illustrated in Figure 3. Each unit cell is connected to three adjacent umbrellas via single-axis rotational joints. In this section, we will describe the unit cell and its kinematic properties in more detail, motivate the use of conformal mapping theory for approximate inverse design, and explain our simulation model.

3.1 Umbrella Unit Cell

An umbrella unit cell consists of two horizontal triangular plates and three scissor linkage mechanisms called *arms* (Figure 4). We refer to the three joints connecting a unit cell with its neighbors as *X-joints* and the joints coupling the arms to the triangular plates as *T-joints* (Figure 4). The plates are equilateral triangles with edge length m (the same in every unit cell to simplify fabrication). The cell height H is defined as the distance between the two plates in the compact state. We further define the top and bottom heights H^t, H^b as the distance from the central plane defined by the three X-joints to the top and bottom plates, respectively. These height values in the rest state are the primary design parameters later optimized by our inverse design algorithm. We define the cell *footprint* as the triangle whose edge midpoints coincide with the three X-joints (illustrated with dashed lines in Figure 3 and Figure 5). Note that in our construction, the cell footprint triangle and the plate triangles are all congruent in the fabrication state.

3.2 Deployment Kinematics

An isolated umbrella cell is deployed by pressing the top and bottom plates together (Figure 3a). This compression drives a zero-energy mode that pushes the X-joints outwards and expands the cell footprint. Upon full compression, the cell footprint edge length increases by $2\sqrt{3}h$, where $h = \min(H^t, H^b)$.

To improve the stiffness of the deployed surface, we can increase its structural depth by deploying to a nonzero target plate separation s_{target}. In this case, the length increase is $\sqrt{12h^2 - 6{s_{\text{target}}}^2}$, implying a length expansion factor of

$$\sigma := \frac{m + \sqrt{12h^2 - 6{s_{\text{target}}}^2}}{m}. \tag{1}$$

Note that increasing h can increase this expansion factor indefinitely.

If identical umbrella cells are linked into a regular equilateral triangle grid, the mesh structure can still expand and contract in-plane in a single-degree-of-freedom motion without elastic deformations: the individual unit cell modes are *compatible* (Figure 3b). However,

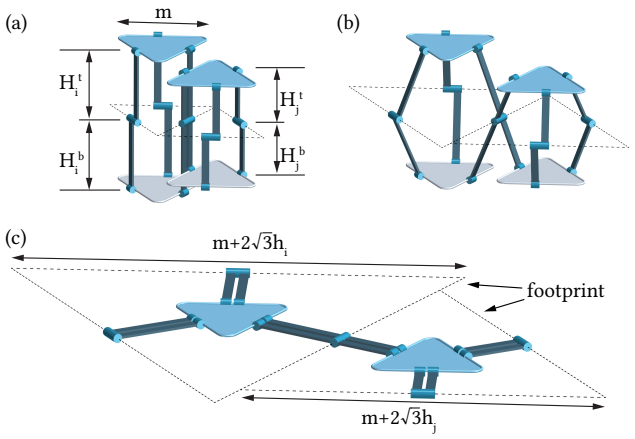

Fig. 5. The heights of the umbrella units or, equivalently, the lengths of the umbrella arms, determine their expansion ratio after deployment. Two umbrellas of different heights expand into footprints of different sizes, which causes incompatibility at their common edge.

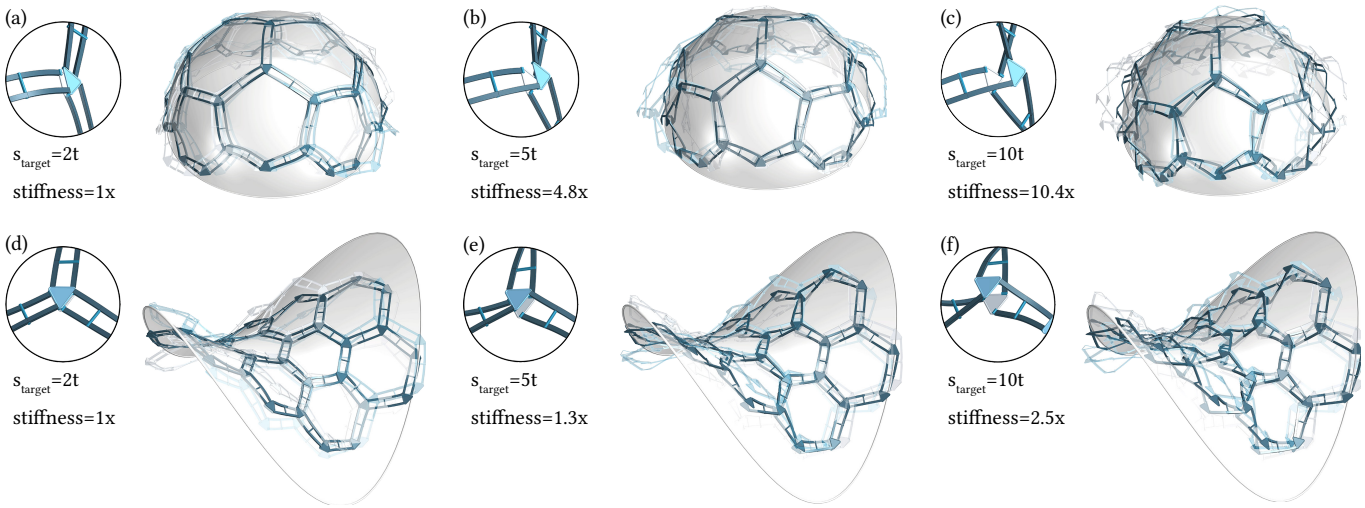

Fig. 6. Structures with different target plate separation s_{target} have different stiffnesses. As we increase s_{target} from twice the thickness of the structure's beams ($2t$) to ten times the thickness ($10t$), we observe increases in structural stiffness. For each design, we visualize its weakest deformation mode.

when umbrellas are assigned differing heights, these expansions generally become incompatible and force the arms to deform elastically. Crucially, these incompatibilities end up buckling the expanded cells out of plane and into a curved configuration (Figure 3c).

3.2.1 Auxetic metamaterials and conformal maps. As seen in our kinematic analysis above, the cell footprints of a regular umbrella mesh without incompatibilities undergo a pure scaling transformation during deployment. This means that, when viewed as a volumetric mechanical metamaterial, regular umbrella meshes are transversely isotropic with an in-plane Poisson's ratio of -1 (and a high positive out-of-plane Poisson's ratio). Varying the umbrella heights slowly relative to the unit cell size produces a metamaterial with spatially varying out-of-plane Poisson's ratios and maximum expansion factors, which in turn encodes the intrinsic curvature of the fully expanded state. In this sense, umbrella meshes are closely related to the 2D auxetic metamaterial systems comprising rigidly rotating triangles or squares that have become popular building blocks for deployable surface structures [Konaković et al. 2016]. However, our volumetric metamaterial has two key advantages. First, the structural depth lends improved stiffness as demonstrated in Figure 6. Second, because material is brought in from out-of-plane during deployment, umbrella meshes can achieve arbitrarily large expansion ratios in theory, which has direct implications for the achievable design space.

The link between expansion ratios and design space is clarified by conformal mapping theory, which also provides an efficient strategy for constructing the umbrella mesh's topology and initializing its shape parameters for our subsequent optimization (Section 5.1).

As observed by Konaković et al. [2016], the perfectly isotropic expansion implied by a Poisson's ratio of -1 means that the material's deformation from a flat sheet to a curved surface is well-approximated by a conformal map f (for umbrella meshes, it is the transformation of the midsurface interpolating the X-joints that is approximated by this map). Any other deformation is strongly resisted. Hence, for a surface to be approximated by a deployable auxetic structure, there must exist a conformal flattening f^{-1} to the fabrication state that respects the limits of the material system. For the rotating triangle and square auxetics, this means that the point-wise length scalings induced by f (the single repeated singular value σ of ∇f at each point) must be less than a factor of 2 and $\sqrt{2}$, respectively—and substantially less for certain fabrication approaches. This limitation strongly restricts what shapes can be approximated. For instance, the largest portion of a sphere that can be conformally mapped to the plane without inserting singularities or exceeding these distortion bounds is a hemisphere; we demonstrate in Section 6 that by lifting scale factor restrictions, umbrella meshes can achieve a significantly richer shape space without the need for cuts or cone singularities.

3.3 Representation

To efficiently simulate the elastically deforming umbrella arms during the deployment transformation, we employ the discrete elastic rods model introduced in [Bergou et al. 2010, 2008]. We couple the elastic beams using a generalized single-rotational-axis joint model that extends the joint model defined by Panetta et al. [2019].

3.3.1 Generic hinge joint. Each joint in our model consists of two hinge leaves that rotate around a single rotation axis (hinge) to form an opening angle α. We define the opening angles to be zero at initialization, corresponding to a fully closed structure (see the illustration in Figure 4). The hinges rotate freely *without storing elastic energy* until they encounter upper or lower angle bound constraints that can be configured separately for each joint. The state of the joint is therefore defined by seven degrees of freedom: the midpoint $\mathbf{q}$ of the hinge axis, the joint orientation $\boldsymbol{\omega}$ (represented as a rotation in axis-angle vector form), and the opening angle α.

Our model allows the terminal edges of any number of discrete elastic rods to be rigidly attached to each hinge leaf at arbitrary orientations and spatial offsets. The rest-state configuration of each

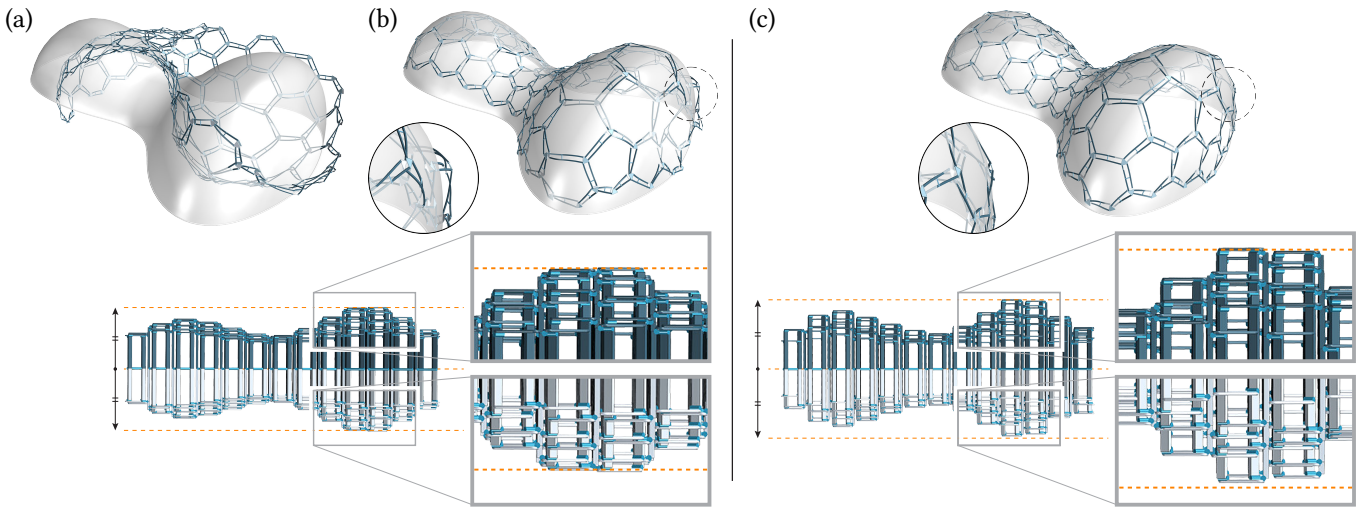

Fig. 7. Encoding mean curvature. When optimized with a single height parameter per umbrella, the structure cannot encode a preference for positive or negative mean curvature and hence sometimes deploys into the wrong shape (a). The limited design space also causes deviation from the target surface even when the structure is deployed correctly (b). The structure optimized with separate top and bottom height variables per umbrella always deploys correctly due to the asymmetry in the compact state and approximates the target surface much better thanks to the extended design space (c).

terminal edge (*i.e.*, the edge tangent, first material frame vector, and the offset from $\mathbf{q}$ to the midpoint) are provided as input to the simulation; in our specific pipeline, these are generated by the initialization scripts described in Section 5.1. Each of these rest configurations is rigidly transformed by the transformation of the hinge leaf to which the edge is bound. The resulting configuration, along with an additional length variable permitting edge stretching, completely determines the terminal edge's deformed state. We eliminate from the simulation the corresponding discrete elastic rod variables (two centerline vertex positions and a material frame angle) by expressing them in terms of the bound joint's parameters using the formulas provided in the supplementary material.

3.3.2 Unit cell model. The triangular plates of an umbrella element are fabricated from a much stiffer material than the arms and remain essentially rigid throughout the deployment. We therefore forego a detailed plate simulation in favor of an abstracted model consisting of three elastic rods joined rigidly at the plate center (see Figure 4b); such rigid connections are achieved in our generalized joint by eliminating the α variable. We set the Young's modulus of these rods to be several orders of magnitude higher than those of the arms and validated that these stiff rods did not sustain appreciable deformation in the deployment simulation.

Figure 4 shows how each connection in the unit cell can be represented by our joint model. To construct X-joints (Figure 4d), we align the weak bending axis of the rods with the joint's rotation axis. To construct T-joints (Figure 4c), we align the strong bending axis of the rod representing the plate (*i.e.*, the plate normal) with the hinge leaf; the angle between the tangent of this rod and the rotation axis depends on the width of the arm assembly. To account for subtractive fabrication processes like milling, where the hinges are formed by removing material from one side of the arm, we offset the rod away from the rotation axis (see Figure 4c and 4d, where the rotation axis lies at the rod surface rather than piercing through its center); for 3D printing, this offset can be zero.

3.3.3 Simulation variables. With our abstract plate model, the full umbrella mesh is ultimately a collection of elastic rods constrained by joints. Accordingly, the simulation problem variables comprise a vector $\mathbf{x}$ concatenating the joint configurations $\mathbf{q}_j, \boldsymbol{\omega}_j, \alpha_j$ with the terminal edge length variables l_e and the discrete elastic rod degrees of freedom $\mathbf{r}_s$ that remain after constraining the terminal edges. Please see the supplementary materials for a more detailed specification of the simulation variables.

3.3.4 Design parameters. In principle, every rod's length and terminal edge orientation/offset could be optimized to tune the deployed shape and its structural properties. However, most values of these parameters are incompatible and would lead to residual stresses in the rest state, complicating assembly and excluding the possibility of direct 3D printing. Furthermore, to facilitate mass-production, we wish to constrain all triangle plates to be identical. We therefore perform our design optimization in a reduced parametric space crafted to include only structures known to have zero-energy fabrication states. Specifically, we select as design variables the same parameters introduced when defining the unit cell: the top and bottom heights H^t and H^b of each umbrella, collected into a vector $\mathbf{p}$.

We note that the ability to separately adjust the top and bottom heights in each umbrella is an important design freedom, enabling us to break the reflectional symmetry of past metric-based inverse design approaches. This allows us to directly encode particular extrinsic curvatures that were previously either limited to a restrictive range by the deployment process (positive mean curvature in [Konaković-Luković et al. 2018]) or left entirely uncontrolled [Chen et al. 2021]. To assess the benefits contributed by this design freedom, we implemented a "single-height" variant of our design parametrization that enforces the constraint $H^t = H^b$ for each umbrella. We

confirm that this restricted approach fails to encode the mean curvature sign (Figure 7) and is less effective at pinning down isometric deformations than the enriched asymmetric design space.

4 FORWARD SIMULATION

Equipped with our discrete model for umbrella meshes, we develop a method for robustly simulating their deployment. Due to our structures' high stiffness-to-mass ratios, we neglect inertial forces and opt for a quasi-static simulation. We formulate the equilibrium problem at a given step in the deployment process as minimizing a total potential energy; this enables us to distinguish stable configurations (local minima) from unstable ones (saddle points) and employ robust numerical solvers.

Our total potential energy includes the elastic energy $\mathcal{E}$ stored in the umbrella mesh as well as a potential energy term $\mathcal{D}$ modeling the deployment forces, a barrier term $\mathcal{B}$ for enforcing angle constraints, and a target-surface attraction term $\mathcal{T}$ used to constrain rigid motion:

$$\mathcal{U}(\mathbf{x}, \mathbf{p}) = \mathcal{E}(\mathbf{x}, \mathbf{p}) + \mathcal{D}(\mathbf{x}) + \mathcal{B}(\mathbf{x}) + \epsilon\mathcal{T}(\mathbf{x}).$$

The elastic energy term simply sums the energies in each constituent discrete elastic rod since the hinges are assumed to rotate freely without deforming. The deployment and barrier terms are described in the following paragraphs, and the target-fitting term (added here with a low weight ϵ) is introduced in Section 5.

While the structure's rigid orientation could be constrained simply by applying pin constraints to a single joint's $\mathbf{q}$ and $\boldsymbol{\omega}$ variables, this has several drawbacks. First, pin constraints initially concentrate elastic energy around the fixed joint that takes many Newton iterations to release by gradually rotating the rest of the structure. More importantly, the position and orientation at which the joint should be fixed relative to the input surface for optimal shape approximation is unknown. Using the target-attraction term effectively incorporates a rigid registration with the target surface into the simulation, simplifying the surface-fitting objective of the design optimization (Section 5). We set ϵ small enough that the nonphysical attraction forces (which are proportional to the deviation from the target surface) are negligible on the optimal design, and we always validate the shape approximation fidelity without fictitious forces (Figure 10) using a final simulation with pin constraints and $\epsilon = 0$.

Linear actuators. To formulate our deployment energy, we introduce a robust virtual *linear actuator* element that attaches to the top and bottom plates of a unit cell and drives them to the target separation s_{target}. A simple zero-length spring would suffice to pull together the plates' centers $\mathbf{q}^t$ and $\mathbf{q}^b$ but cannot be used to drive the plates to $s_{\text{target}} \neq 0$ (*e.g.*, Figure 6) or avoid collisions of one plate with another. A nonzero-length spring (a potential energy term like $(\|\mathbf{q}^t - \mathbf{q}^b\| - s_{\text{target}})^2$) would be problematic since it is unstable under compression and risks pushing through to an inverted zero-energy state. Our linear actuator addresses these robustness issues while preventing collisions and naturally modeling the forces applied by the passive spacers used in our fabricated deployed structures.

Denoting the (oppositely oriented) normals of the top and bottom plates by $\mathbf{n}^t$ and $\mathbf{n}^b$, we define the deployment unit axis vector $\mathbf{a} := \text{normalize}(\mathbf{n}^t - \mathbf{n}^b)$. We then decompose the vector connecting the plate centers into its components parallel and perpendicular to $\mathbf{a}$, obtaining the normal separation $\mathbf{a} \cdot (\mathbf{q}^t - \mathbf{q}^b)$ and tangential deviation $(I - \mathbf{a} \otimes \mathbf{a})(\mathbf{q}^t - \mathbf{q}^b)$, respectively. Our actuator seeks to fit the former to s_{target}. It further minimizes the tangential deviation to stabilize the deployment simulation of designs in their initial steps of optimization (when plates might otherwise shear into bad configurations) and to model the frictional contact forces applied by the spacers. Finally, the actuator enforces alignment of the top and bottom plate normals, which, together with the prescribed separation, prevents plate collisions. Note that our design optimization will subsequently tune the forces these virtual actuators apply to values that can be supplied by passive rigid spacers (Section 5.2.3), promoting structures that remain in equilibrium when active deployment forces are removed.

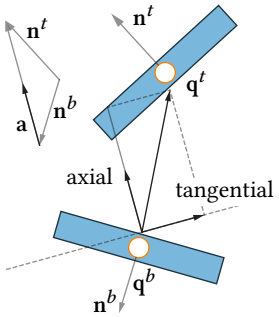

We define the energy of a single linear actuator as:

$$\begin{aligned}\mathcal{L}(\mathbf{n}^t, \mathbf{n}^b, \mathbf{q}^t, \mathbf{q}^b) = &\frac{1}{2} w_1 \left\| \mathbf{n}^t + \mathbf{n}^b \right\|^2 \\ &+ \frac{1}{2} w_2 \left\| (I - \mathbf{a} \otimes \mathbf{a})(\mathbf{q}^t - \mathbf{q}^b) \right\|^2 \\ &+ \frac{1}{2} w_3 (\mathbf{a} \cdot (\mathbf{q}^t - \mathbf{q}^b) - s_{\text{target}})^2.\end{aligned}$$

As $\mathbf{n}^t$ and $\mathbf{n}^b$ are constrained to be unit length by construction (they are given by the orientation variable of the central joint of our abstracted plate model), we apply the simplification $\|\mathbf{n}^t + \mathbf{n}^b\|^2 = 2\mathbf{n}^t \cdot \mathbf{n}^b + \text{constant}$. We obtain the full deployment potential energy term for our simulation by summing the energy of each actuator over the umbrellas: $\mathcal{D} = \sum_i \mathcal{L}(\mathbf{n}_i^t, \mathbf{n}_i^b, \mathbf{q}_i^t, \mathbf{q}_i^b)$.

Joint angle constraints. Our physical joints impose constraints on the opening angles α that are crucial for faithfully predicting the deployed shape. Specifically, the angles at the X-joints are constrained to the interval $[0, \pi]$, and the angles at the T-joints are constrained to $[0, \pi/2]$. For pure simulation, these constraints can be implemented efficiently as bound constraints in the optimizer. However, this makes the equilibrium deformation a non-differentiable function of the design parameters at the point where the bounds are encountered or released. The consequent discontinuities in the design gradient are unfortunately widespread in our experiments and inhibit design optimization (Section 5.2.4).

We address this issue by reformulating the angle bound constraints of the form $c_i \leq 0$ using C^2 barrier terms that smoothly activate and penalize the constraint violation:

$$\mathcal{B} := \sum_i \left(\log\left(\frac{b - a}{b - c_i} \right) \right)_+^3,$$

where a is the threshold above which the penalty activates, b is the location of the infinite energy barrier, and $(\cdot)_+$ clamps to the non-negative real numbers. We fixed $a = -0.02$ and $b = 10.0$, which for the scale of our models struck a good balance between graceful

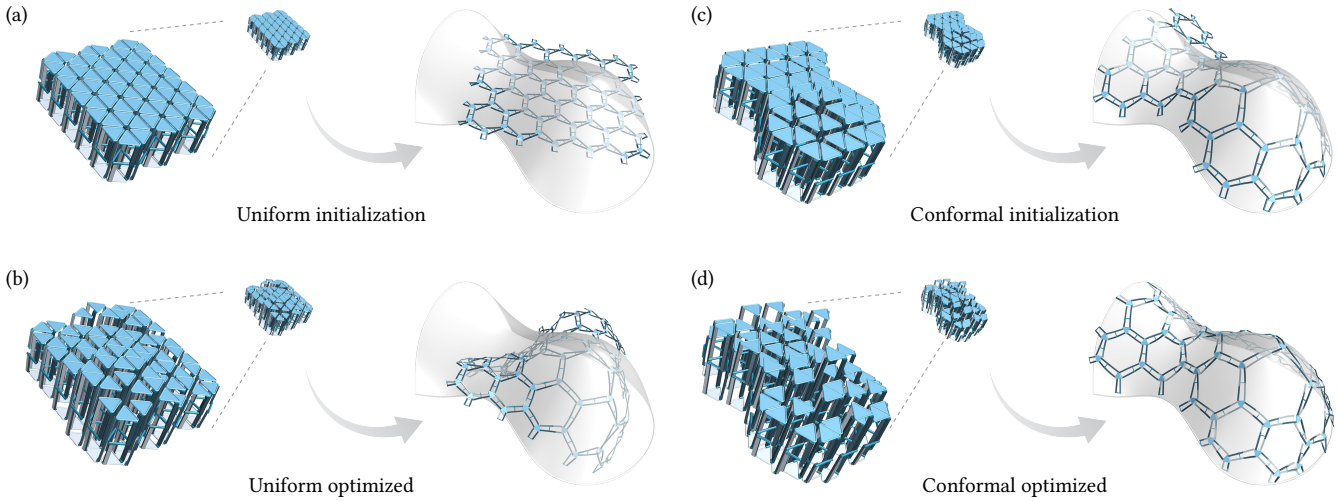

Fig. 8. When initialized with a regular patch of identical umbrellas (a), the design optimization tends to get stuck in bad local minima (b). In contrast, the optimization performs much better (d) when we compute the rest state topology using conformal flattening and initialize the umbrellas heights using the conformal scale factors (c).

activation and excessive constraint violations. Physically speaking, this relaxation can be interpreted physically as a slight elasticity in the hinges.

Full formulation. Our simulation algorithm consists of the following constrained minimization of total potential energy:

$$\mathbf{x}^*(\mathbf{p}) = \underset{\substack{\mathbf{x} \\ l_e \geq \epsilon \ \forall e}}{\operatorname{argmin}} \mathcal{U}(\mathbf{x}, \mathbf{p}).$$

We retain bound constraints on the terminal edge length variables l_e to prevent collapses or inversions of these edges at intermediate steps of the minimization, but we note that these bounds are never active in the equilibrium state. Therefore their inclusion poses no differentiability issues.

This simulation can be run in two modes: (i) to obtain a physically meaningful estimate of the deformation and elastic energy at each step of the process; or (ii) to quickly solve for the deployed state only. For (i), we run a sequence of simulations with intermediate target plate separation values set individually for each umbrella (*e.g.*, linear interpolating between the differing starting cell heights and the globally imposed s_{target}). For (ii), we set the full target plate separation at once and attempt to solve a single optimization problem with a high deployment weight. Using the energy limiting strategy described below, this often succeeds. For difficult deployments, we lower the weight on the deployment term and then incrementally return it to full force over a small number of solves. In practice, we found three of these optimization rounds sufficed for nearly every model except the one shown in Figure 11c, which required six rounds. The full simulation process takes less than 40*s* on our most intricate model (Figure 17).

Equilibrium solver. We solve the minimization problem using a Newton-based solver similar to the one described in [Panetta et al. 2019]. To handle the indefinite potential energy Hessian matrix encountered at several stages of the deployment (especially as the structure buckles out of its initial planar configuration), we modify the Hessian by adding a scaled multiple of the full (non-lumped) mass matrix M, which is assembled from the individual discrete elastic rods mass matrices. To escape unstable equilibria, we perturb the deformed configuration in a direction of negative curvature found by computing the eigenvector corresponding to the most negative eigenvalue.

The designs generated by our initialization algorithm can require significant forces to deploy, meaning a large weight must be placed on the deployment energy term for the target plate separation to be tightly enforced. Naïvely attempting to minimize $\mathcal{U}$ from the closed state would result in a large Newton step in the first iteration that puts the structure in an often unrecoverably bad configuration. This happens despite a line search: the closed state has an extremely high deployment energy that gets traded for elastic energy in the first step. In lieu of a more sophisticated numerical continuation method, we find that a simple "energy limiting" heuristic achieves rapid progress towards the deployed state without overstraining the structure: We impose a maximum factor by which the elastic energy is allowed to increase in a single iteration. We assign an infinite energy value to steps exceeding this factor, which forces our line search to backtrack to a more reasonable configuration. We found through experiments that setting the limit on elastic energy increase to $2 - 5\times$ gives the best convergence rates.

Stiffness analysis. Once structures reach equilibrium, their stiffnesses can be evaluated by solving a generalized eigenvalue problem,

$$\frac{\partial^2 \mathcal{U}}{\partial \mathbf{x}^2}\mathbf{v} = \lambda M \mathbf{v},$$

for the smallest nonzero eigenvalue λ of the total potential energy Hessian omitting the $\epsilon\mathcal{T}$ term. Physically, λ quantifies the proportionate restoring force felt when infinitesimally perturbing the

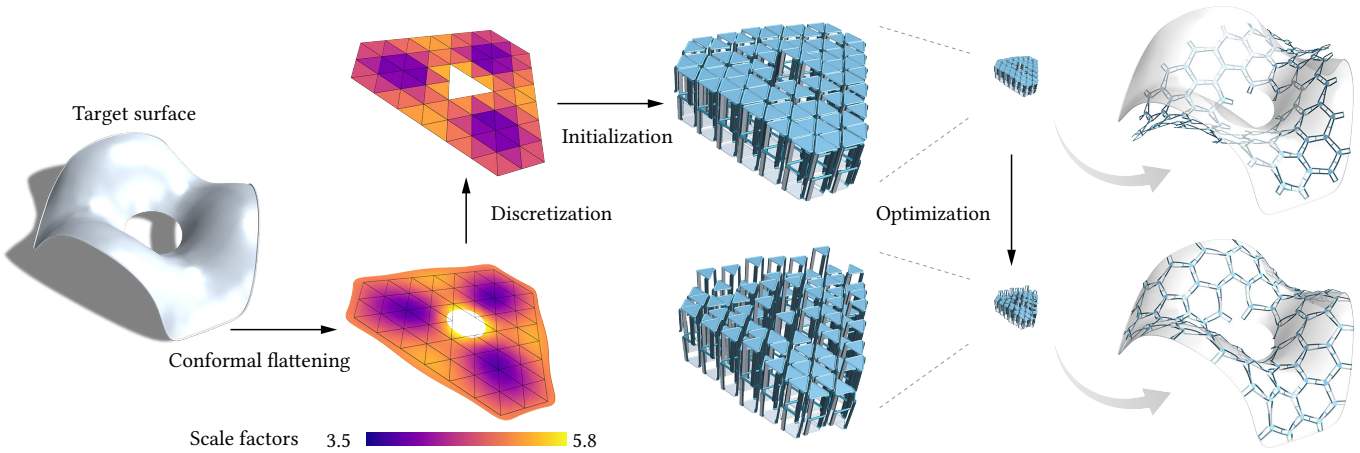

Fig. 9. Computational pipeline. The input to our inverse design pipeline is a target surface. We compute a conformal flattening of the surface to the plane and initialize a regular grid of umbrellas of varying heights using the conformal scale factors. We preview the deployed shape of this initialization by running our simulation algorithm and then apply our design optimization algorithm to find optimal height parameters. The deployed shape of the optimized result closely approximates the target surface.

structure out of its equilibrium along the corresponding direction of least stiffness $\mathbf{v}$. We use this analysis to numerically confirm one of the main advantages of umbrella meshes, that their structural depth provides enhanced stability. In Figure 6, we show that for both the hemisphere and saddle shapes, as we increase target plate separation s_{target} from twice the rod thickness ($2t$) to five times ($5t$) and ten times ($10t$), the stiffness of both structures increases substantially. The increase is especially prominent for surfaces of positive Gaussian curvature that are otherwise prone to near-isometric deformations unless their boundaries are constrained.

5 DESIGN ALGORITHM

Our inverse design optimization solves for an umbrella mesh to best approximate a smooth freeform input surface (Figure 9). The algorithm proceeds in two phases: We first construct an initial design according to the geometric abstraction of the linkage's in-plane behavior as a conformal map. This abstraction misses several key aspects of the physical system, but it provides the umbrella mesh topology and a reasonable initialization of the height parameters. Then in the second phase we perform physics-based shape optimization that directly maximizes the relevant performance metrics.

5.1 Geometry-based initialization

The first phase of our algorithm closely resembles the pipelines of past deployable auxetic metamaterial design works [Chen et al. 2021; Konaković-Luković et al. 2018]: We first conformally flatten the triangulated input surface $\mathcal{S}$ to the plane, computing a piecewise linear map $f^{-1} : \mathcal{S} \to \mathbb{R}^2$. Then we overlay a coarse regular equilateral triangle grid and clip it to the flattened mesh boundary. Each triangle of this grid becomes the footprint of an umbrella unit cell. The unit cells for adjacent triangles are connected as illustrated in Figure 3. We calculate the conformal scale factor for each coarse triangle by sampling the conformal lifting f at its vertices to obtain a coarse piecewise linear field $\tilde{f}$ and calculating $\sigma = \sqrt{\det\left(\nabla\tilde{f}^{\top}\nabla\tilde{f}\right)}$. Finally, we invert the kinematic relationship in (1) to determine the appropriate (single) umbrella height. In Figure 8, we show that without this conformal flattening initialization, the subsequent design optimization easily gets stuck in bad local minima.

This phase is implemented in Rhino3D [McNeel et al. 2010] as a Grasshopper plugin to facilitate interactive feedback from the user. In particular, the user can adjust the scale, position, and orientation of the overlaid equilateral triangle grid—controlling the resolution, boundary shape, and rough beam alignment of the design—and specify on which portions of the design boundary should the *boundary arms* (arms not connecting with neighboring unit cells) be retained or eliminated. For instance, the top two models of Figure 10 were designed without boundary arms, while the third includes them.

5.2 Shape optimization

The conformal-mapping-based geometric initialization considers only the kinematic behavior of isolated umbrella unit cells. It does not account for the complicated interplay of bending, twisting, and stretching forces in the beams due to incompatibility, nor the out-of-plane stiffness of our material system that enables sturdy structures and control of mean curvature. Furthermore, it is not obvious how to introduce asymmetry in the umbrella design heights in the initialization stage since the appropriate factors would depend on the interaction with neighboring umbrellas and are therefore non-local. Finally, the geometric abstraction is unable to accurately predict and tune the necessary actuation forces to obtain a free-standing structure. To address all of these limitations, we perform a physics-based shape optimization to tune the umbrella height design parameters $\mathbf{p}$ (Section 3.3.4). This process is essential to obtain high-quality results exploiting the full advantages of the umbrella mesh material system. However, shape optimization is generally only successful in combination with our geometry-based initialization (Figure 8).

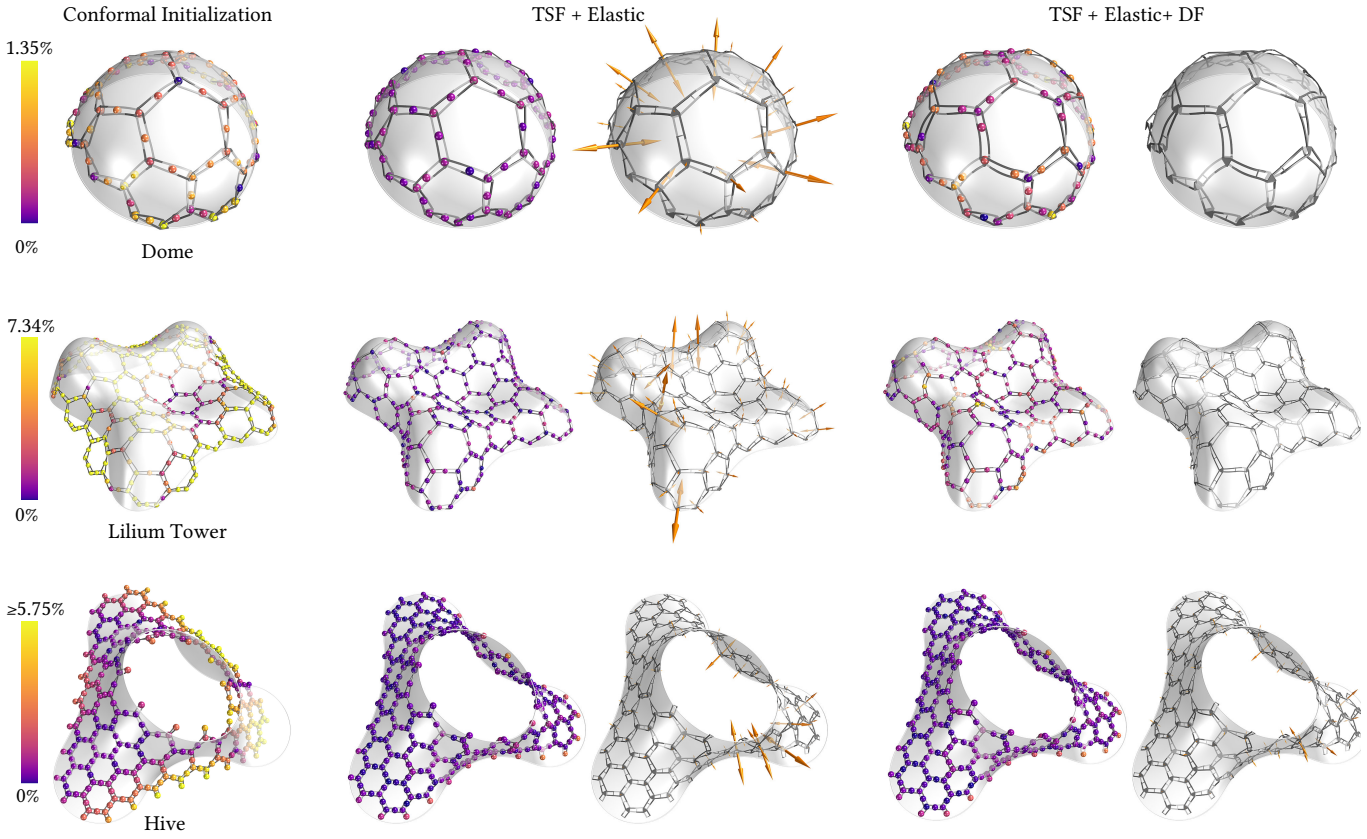

Fig. 10. Design objective ablation studies. We visualize the effects of our target surface fitting (TSF) and deployment force (DF) objectives on three example shapes. The conformally initialized structures deviate from the target surface when deployed. We measure the deviation relative to the bounding box diagonal of the target shapes. For the Dome, Lilium Tower, and Hive, the maximum deviations are 1.346%, 7.337%, and 8.967% (colors are saturated at the maximum values specified in the color bars). After optimizing with the target surface fitting and elastic energy objective terms, the maximum deviations are reduced to 0.247%, 0.780%, 3.125%. The third and fifth columns visualize the tensile elastic forces on umbrella plates. After optimizing with the deployment force objective term as well, all tensile forces are removed for the dome example; in the Lilium Tower and Hive, the forces are significantly reduced. In the force visualization, the vector lengths are proportional to the magnitude of the separation forces at the umbrella units. Some surface approximation quality is traded for tensile force removal in the fourth column, but the deviations are still much smaller than in the initialized design: 1.288%, 1.715%, 3.126%.

5.2.1 Design objectives. We have three primary goals in designing an umbrella mesh: (i) it should deploy to a close approximation of the input surface; (ii) it should be subjected to as little strain energy as possible during deployment; and (iii) it should remain in its deployed state without external constraints or actuation. Each of these goals is formulated as a term in the full objective of our design optimization:

$$J(\mathbf{p}) = \mathcal{T}(\mathbf{x}^*(\mathbf{p})) + \mathcal{E}(\mathbf{x}^*(\mathbf{p}), \mathbf{p}) + \hat{\mathcal{D}}(\mathbf{x}^*(\mathbf{p}), \mathbf{p}).$$

The terms $\mathcal{T}(\mathbf{x}^*(\mathbf{p}))$ and $\mathcal{E}(\mathbf{x}^*(\mathbf{p}), \mathbf{p})$ are the same as in the simulation's potential energy, representing deviations from the input surface and the stored elastic energy respectively, but note that they are *evaluated at the equilibrium configuration* $\mathbf{x}^*(\mathbf{p})$ corresponding to the design parameters $\mathbf{p}$. The third term $\hat{\mathcal{D}}$ promotes beneficial deployment forces; it is distinct from the related potential energy term $\mathcal{D}$ and is defined below. Evaluating any of these terms for a particular design candidate $\mathbf{p}$ requires running the equilibrium solve in an inner loop. These terms and the overall optimization framework are similar to [Ren et al. 2021] but have been customized for the specific design considerations of umbrella meshes.

5.2.2 Target surface fitting. Since we generally deploy the umbrella mesh with a nonzero s_{target}, we must define which parts of the structure are intended to lie on the target surface. We choose the X-joint positions as well as the *average* of the top and bottom plate joint positions for each umbrella; both sets of points visually lie on the structure's implied midsurface. We collect these midsurface point coordinates into a large vector $\mathbf{m}(\mathbf{x})$, which is a linear function of the deformed configuration state. We further distinguish between *boundary* midsurface points $\mathbf{m}_b$ (originating from boundary arm X-joints) and *interior* midsurface points $\mathbf{m}_i$ (all the rest).

We minimize the distance between the midsurface points and their closest points on $\mathcal{S}$, where the closest point to each boundary midsurface point is constrained to lie on the boundary. To prevent the structure from crumpling or shifting significantly on the target

surface, we also penalize the deviation from the initial positions $\overline{\mathbf{m}}_i$ of $\mathbf{m}_i$, which are computed by lifting the midsurface points to $\mathcal{S}$ by f. Note that the initial positions of $\mathbf{m}_b$ are generally in poor locations and hence ignored since it is unusual for the coarse triangle grid boundary to coincide with the input surface boundary ∂S.

The full definition of the surface fitting function is as follows:

$$\mathcal{T}(\mathbf{x}) = \|\mathbf{m}_i - P_{\mathcal{S}}(\mathbf{m}_i)\|^2_{W_i} + \|\mathbf{m}_i - \overline{\mathbf{m}}_i\|^2_{W_i} + \|\mathbf{m}_b - P_{\partial\mathcal{S}}(\mathbf{m}_b)\|^2_{W_b},$$

where $P_X(\mathbf{y})$ denotes the operator projecting the points represented by the vector $\mathbf{y}$ to their closest points in the set X. Note that each term is measured with a weighted norm to allow the user to specify not only the relative importance of, *e.g.*, fitting the boundary points, but assign a spatially varying importance value to the points of $\mathbf{m}$.

5.2.3 Deployment force objective. Even if the optimizer is able to fit the simulated equilibrium closely to the target surface and with a low strain energy, the structure may deflect away from the target surface when the potentially high virtual actuation forces are removed—or worse, fully retract to its rest state. Fortunately, we have observed that umbrella meshes are generally *bistable*, and we can optimize them to become stable in the absence of active deployment forces without appreciably sacrificing surface approximation quality. This is the purpose of $\hat{\mathcal{D}}$: to minimize the components of the actuation force that cannot be applied passively.

Our physical models feature 3D printed spacers that are inserted between the top and bottom plates to maintain the target separation of s_{target}. Assuming that the plate separation spring of a linear actuator in our simulation model is under compression and that the other springs are not excessively strained, the actuator can be replaced by a passive spacer: it will be held in place by Coulomb friction and will maintain the target plate separation. Conversely, if that spring is under tension, or if there is significant tangential force or torque acting on the linear actuator, the umbrella will not be stable.

We ensure beneficial forces by considering every plate in the umbrella mesh (top and bottom) one at a time. The force applied to the linear actuator by the plate associated with central joint j is $-\frac{\partial \mathcal{E}}{\partial \mathbf{q}_j}$. We decompose this force into tangential and normal components along the actuator axis $\mathbf{a}$. To simplify our formulas slightly, we assume that the actuator constraints are tightly enforced so that $\mathbf{a} \approx \pm\mathbf{n}_j$, making the *compressive* force $f_j^c := \frac{\partial \mathcal{E}}{\partial \mathbf{q}_j} \cdot \mathbf{n}_j$. Similarly, the tangential force is $f_j^t := \left\| \frac{\partial \mathcal{E}}{\partial \mathbf{q}_j} \right\|^2 - \left(f_j^c\right)^2$, and the torque applied by the plate is $\tau_j := -\frac{\partial \mathcal{E}}{\partial \boldsymbol{\omega}_j}$. With these expressions, we can formulate our objective term as a sum over the plate joints:

$$\hat{\mathcal{D}} = \sum_{j \in \mathcal{P}} w_c \left(c_{\min} - f_j^c\right)_+^2 + w_t \left(f_j^t\right)^2 + w_\tau \left\|\tau_j\right\|^2,$$

where $c_{\min} \geq 0$ is the minimum allowable compressive force, and w_c, w_t, w_τ are weights.

It is tempting to replace, *e.g.*, $\frac{\partial \mathcal{E}}{\partial \mathbf{q}_j}$ with the considerably simpler expression $-\frac{\partial \mathcal{D}}{\partial \mathbf{q}_j}$ that involves only deformation variables and not elastic energy derivatives. After all, the vanishing gradient $\frac{\partial \mathcal{U}}{\partial \mathbf{q}_j}$ at equilibrium means these expressions differ only by the negligible quantity $\epsilon \frac{\partial \mathcal{T}}{\partial \mathbf{q}_j}$. However, this replacement causes numerical stability issues for evaluating $\hat{\mathcal{D}}$ and especially its derivatives: as simulation constraint penalty weight w_3 increases, the plate separation approaches s_{target}, and the force expression $-\frac{\partial \mathcal{D}}{\partial \mathbf{q}_j}$ suffers from cancellation error. This is especially problematic since the equilibrium state variables cannot be computed with extreme accuracy.

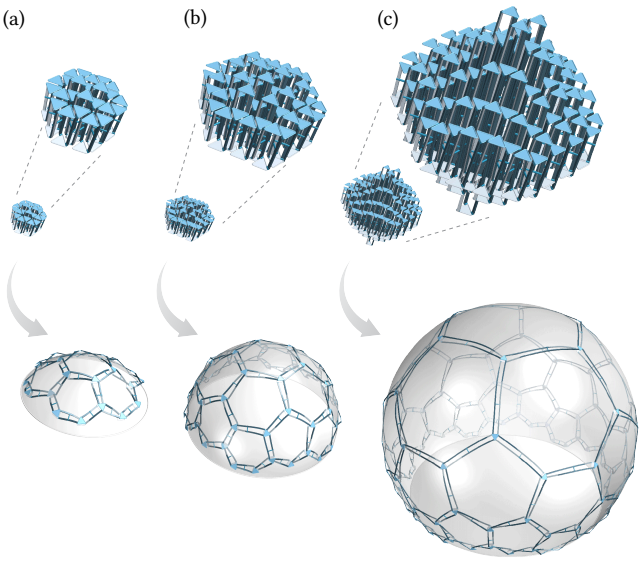

Fig. 11. Scale factors. Umbrella meshes can achieve in principle arbitrarily high expansion ratios. In particular, we are able to design an umbrella mesh that deploys into a spherical patch covering more than a hemisphere, which is the limit of previous conformal deployable structures [Chen et al. 2021; Konaković-Luković et al. 2018]. For the three spherical caps shown here, the maximum-to-minimum scale factor ratios are 1.41, 2.09, and 5.19.

5.2.4 Numerical shape optimization. Our shape optimization is formulated as the nonlinear minimization:

$$\min_{\substack{\mathbf{p} \\ p_i \geq H_{\min}\ \forall i}} \quad J(\mathbf{p}),$$

where the bound constraints enforce a minimum umbrella height. We employ the Newton-CG algorithm implemented in Knitro [Artelys 2021] to rapidly converge to an optimal design. At every design iteration this requires: (i) solving the equilibrium problem for $\mathbf{x}^*(\mathbf{p})$ to evaluate the objective; (ii) evaluating the design gradient $\frac{\partial J}{\partial \mathbf{p}}$; and (iii) computing a number of Hessian-vector products $\frac{\partial^2 J}{\partial \mathbf{p}^2}\delta\mathbf{p}$ (measuring the change in the design gradient along various design perturbations). We use the adjoint method to efficiently calculate the analytical gradients and compute the Hessian-vector products using second-order sensitivity analysis with the assistance of automatic differentiation for the third-order derivatives of $\mathcal{U}$ that arise. Please refer to [Panetta et al. 2019] for more details on this first- and second-order sensitivity analysis and see the supplement for the necessary derivative formulas for our particular simulation model.

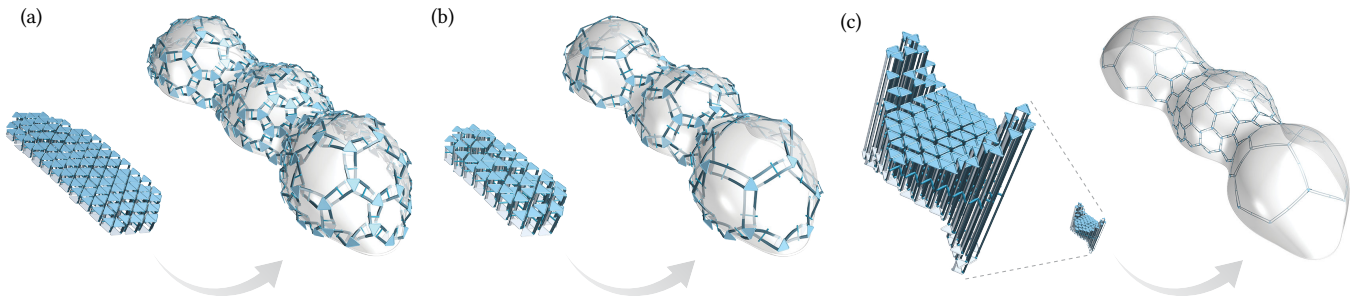

Fig. 12. Design freedom. A single target surface can be realized by umbrella meshes with different geometries. By tuning the conformal map, designs are created (a) with a larger footprint and shorter umbrellas; (b) with a smaller footprint and taller umbrellas; and (c) with a prescribed rhombic footprint shape.

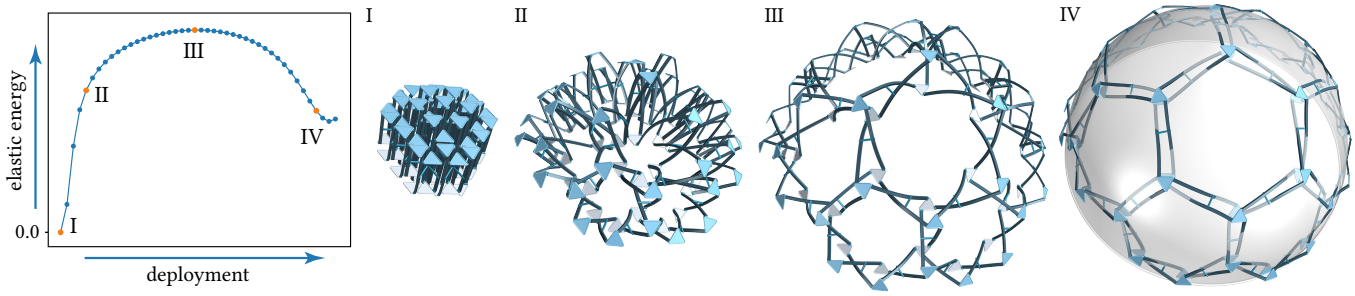

Fig. 13. Bistability. We visualize the elastic energy in the hemisphere as it incrementally deploys to the target plate separation at state IV, noting an energy barrier separating the rest and deployed states. We further extend the deployment past the equilibrium; the energy decrease implies spacers are in compression.

6 RESULTS AND DISCUSSION

Unbounded scale factors. Umbrella meshes transfer material not just in-plane, as surface-based auxetic materials do, but transversally by rotating the umbrella arms from their initial vertical state towards the midsurface during deployment. Consequently, we can theoretically achieve arbitrary area expansion as we increase the heights of the umbrellas. This has important implications for fabricating surfaces with high curvature. For example, we are able to optimize for a structure that deploys into a spherical patch exceeding a hemisphere (Figure 11), surpassing the fundamental limits of the material systems in several past works ([Konaković-Luković et al. 2018; Panetta et al. 2021]).

Enhanced design freedom. Lifting the bounds on the scale factors unlocks additional design freedom even for geometries that could be produced by prior approaches. The conformal flattening used in our pipeline's initialization stage is not unique: it can be composed with a planar conformal map to achieve a desired boundary shape or aspect ratio of the compact state or to tailor the umbrella mesh's spatially varying resolution. The only limit is the scale distortion permitted by the material system. In Figure 12, we illustrate designs trading off between the height and the footprint area of the compact state. Figure 12c shows an example where the Boundary First Flattening software [Sawhney and Crane 2017] was used to reshape the footprint to approximate a rhombus.

Symmetry and mean curvature. Most existing surface-based programmable structures encode only the intrinsic curvature of a target surface ([Chen et al. 2021; Konaković-Luković et al. 2018]). Umbrella meshes can encode the mean curvature of the target surface as well by introducing asymmetry in the top and bottom heights of each umbrella. In Figure 7 we show an example where optimizing only for a single height parameter per umbrella produces a structure that sometimes deploys with the wrong mean curvature. In contrast, umbrella meshes optimized with separate top and bottom height variables are able to encode the proper mean curvature and reliably deploy into the correct target shape with even better shape approximation fidelity. This property shows promise for fully automated deployment via local actuation.

Bistability and deployment force optimization. We have observed that most umbrella meshes are bistable during simulation and in physical deployment. To investigate this numerically, we compute the elastic energy $\mathcal{E}$ throughout the deployment sequence. A precise analysis requires knowledge of the specific deployment path which can be application dependent. As an approximation, we consider the path where the umbrella's individual target plate separation are linearly interpolated from their initial separation toward the global deployment target. We visualize the elastic energy at each of these steps for the dome in Figure 13. All examples shown in this paper have a similar curve. This plot implies the existence of an energy barrier between the undeployed state and deployed state, which means that once the structure is deployed, it will not collapse to the rest state when actuation forces are removed. When we extrapolate past the target spacing, we find the energy initially

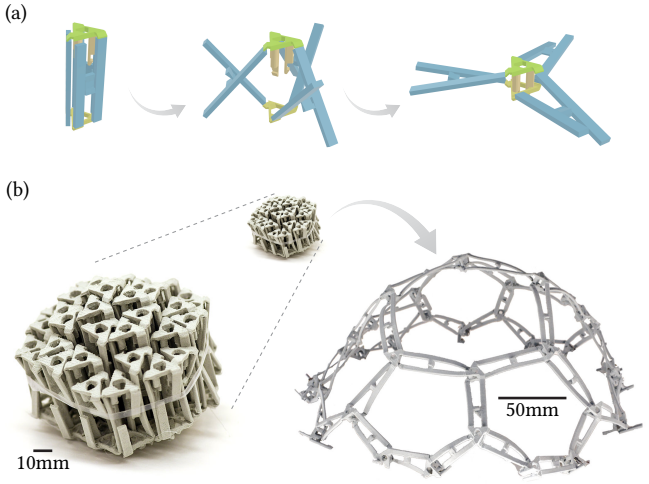

Fig. 14. Umbrella meshes have a zero-energy rest state, so they can be compactly fabricated in one single piece using, for example, SLS 3D printing.

continues to decrease; this is because the structure was optimized to apply compressive forces to its spacers and would relax into an over-deployed state if the spacers were removed. Further demonstrations of deployment force optimization are shown in Figure 10.

6.1 Fabrication

Umbrella meshes can be physically realized in various forms. Figure 14 illustrates the potential for single-piece 3D printing, an attractive approach that efficiently utilizes the 3D print volume and requires no manual assembly. For larger models (Figure 15, Figure 16), we propose an alternative system combining 2D milling and manual assembly: each pair of arms (Figure 15a) is made of 3mm-thick polypropylene on which the X-joint hinge is CNC milled to a depth of 2.6mm, leaving a thickness of 0.4mm for the flexure joint. The top and bottom triangular plates (Figure 15b) are CNC milled from a 6mm-thick PMMA (Acrylic) sheet. The arms are then clipped into the plates (Figure 15c) through a friction fit during assembly. Please see the supplementary materials for details about the machines and materials we used to fabricate our physical models.

6.2 Validation

To evaluate our deployment simulation and inverse design algorithm, we scanned a physical prototype using the Agisoft Metashape photogrammetry software. As shown in Figure 15, the simulated and fabricated models are in close agreement: the maximum deviation of the physical model from the target surface is 5.1% of the bounding box diagonal, and average deviation is 1.3%.

6.3 Limitations and Future Work

In our experiments, we have occasionally observed that some objectives can only be achieved with greater design freedom. There are several promising avenues for expanding the design space that we intend to pursue in future work. First, the constraint that X-joints lie on the same plane in their rest states can be relaxed to introduce additional arm length variables in each unit cell. However, to preserve a zero-energy rest state, an additional integrability condition is required around each hexagon, and the differing heights may cause the top and bottom plates to shear apart slightly when compressed. Second, we can optimize the dihedral angle between umbrella arms, which is currently fixed at 120° (Figure 15c). Our experiments suggest relaxing this constraint will enable the optimizer to reduce stresses in the umbrella arms. However, this relaxation will introduce new challenges in the fabrication setup, and the arms may collide in the rest state if the angle changes significantly. Third, the central design decision in our approach of considering regular equilateral triangle grid topologies could rule out interesting designs that might be achievable with other topologies. While the geometric abstraction allowing us to leverage conformal mapping theory for design initialization unfortunately relies on this grid topology, it would be interesting to explore other initialization strategies.

Our design optimization currently neglects gravitational forces, although these are straightforward to include in our framework by adding another potential energy term to $\mathcal{U}$.

We observed that our physical prototypes often can be deployed by actuating only a few select umbrellas. We are able to simulate partial actuations in our framework, but finding the best actuation locations or actuation sequence to deploy robustly to a target surface is still an interesting open problem. For complex shapes, applying different actuation sequences might lead to different deployed shapes. Moreover, active control the actuation of individual umbrellas or their constituent beams might enable umbrella meshes that morph between various target shapes.

Finally, a very interesting future research direction is to explore combining umbrella meshes into multi-layered structures or coupling umbrella meshes with other compliant elements such as tensile membranes (Figure 17).

7 CONCLUSION

Umbrella meshes offer crucial advantages over existing surface-based deployable structures. By re-distributing material transversally into the surface during deployment, umbrella meshes are not limited in local expansion factor, which provides greater flexibility to achieve complex freeform target states. This also leads to a highly compact undeployed state that offers benefits in storage and transportation and is critical for a number of applications. The price to pay is a more complex fabrication and assembly process, e.g. compared to kirigami structures that can be laser-cut from a single sheet. However, we believe that the principle of out-of-plane material transfer can be explored within many other material systems, opening up interesting avenues for future research.

ACKNOWLEDGMENTS

We are grateful to Filip Goč for helping with the fabrication of physical prototypes. We also thank the anonymous reviewers for their valuable feedback. This research was supported by the Swiss National Science Foundation (Grant FNS 514543 / CF 1156).

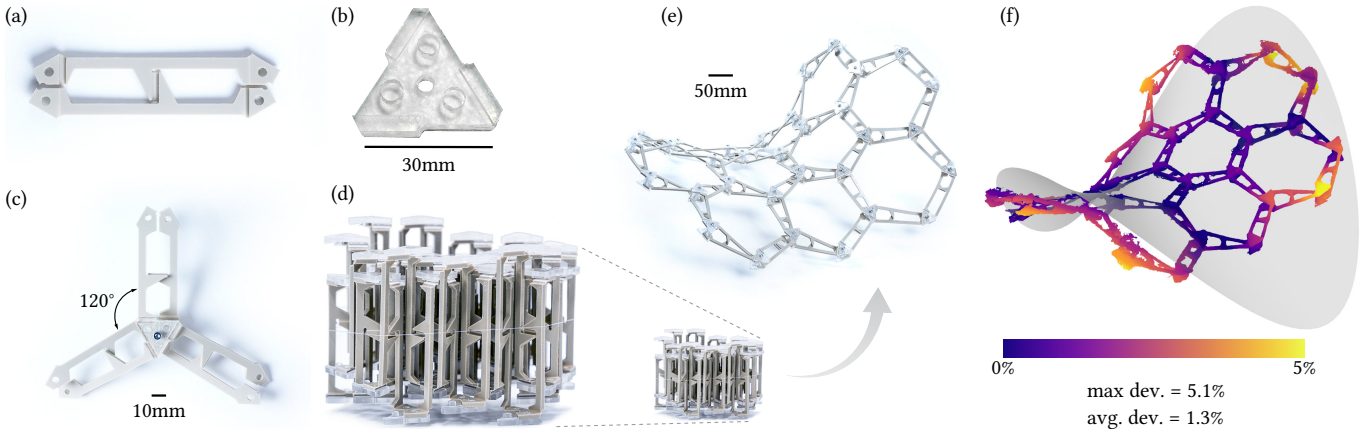

Fig. 15. Physical prototypes and scanning validation. (a) Umbrella arm module; (b) umbrella triangle plate module; (c) a single assembled umbrella module; (d) physical prototype of the saddle in its undeployed state; (e) deployed saddle prototype; (f) validation scan of the deployed saddle. We measure the deviation from the scan of the physical model to the target design surface relative to the surface's bounding box diagonal.

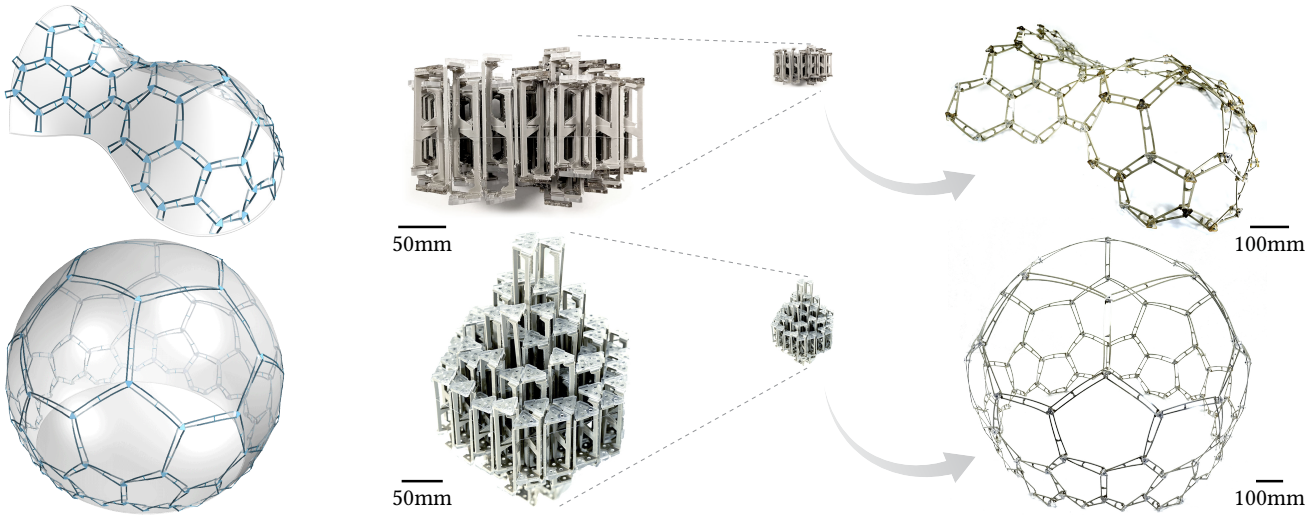

Fig. 16. A showcase of our fabricated models next to their simulated counterparts.

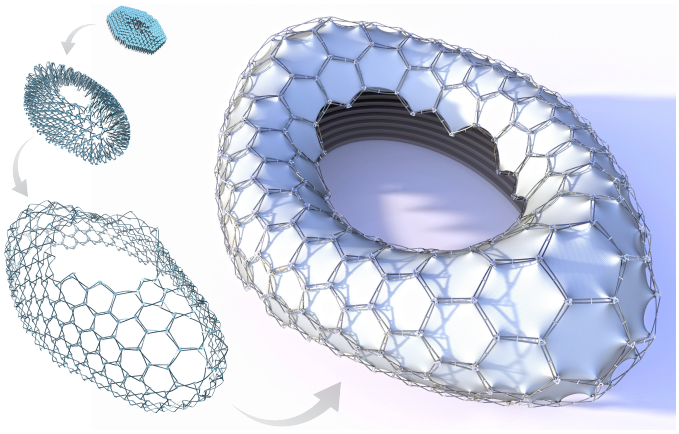

Fig. 17. We envision architectural-scale applications of umbrella meshes, potentially coupled with tensile membranes, as future work.

REFERENCES

LIW Arnouts, Thierry J Massart, Niels De Temmerman, and PZ Berke. 2018. Computational modelling of the transformation of bistable scissor structures with geometrical imperfections. *Engineering Structures* 177 (2018), 409–420.

Artelys. 2021. Artelys Knitro - Nonlinear optimization solver. https://www.artelys.com/en/optimization-tools/knitro

Miklós Bergou, Basile Audoly, Etienne Vouga, Max Wardetzky, and Eitan Grinspun. 2010. Discrete viscous threads. *ACM T Graphic* 29, 4 (2010), 116.

Miklós Bergou, Max Wardetzky, Stephen Robinson, Basile Audoly, and Eitan Grinspun. 2008. Discrete elastic rods. *ACM T Graphic* 27, 3 (2008), 63.

B. Bickel, M. Baecher, M. Otaduy, W. Matusik, H. Pfister, and M. Gross. 2009. Capture and Modeling of Non-Linear Heterogeneous Soft Tissue. *Proc. ACM SIGGRAPH02+* 28, 3 (2009).

Tian Chen, Osama R Bilal, Robert Lang, Chiara Daraio, and Kristina Shea. 2019. Autonomous deployment of a solar panel using elastic origami and distributed shape-memory-polymer actuators. *Physical Review Applied* 11, 6 (2019), 064069.

Tian Chen, Julian Panetta, Max Schnaubelt, and Mark Pauly. 2021. Bistable auxetic surface structures. *ACM Transactions on Graphics (TOG)* 40, 4 (2021), 1–9.

Xiang Chen, Changxi Zheng, Weiwei Xu, and Kun Zhou. 2014. An Asymptotic Numerical Method for Inverse Elastic Shape Design. *ACM Trans. Graph.* 33, 4, Article 95 (jul 2014), 11 pages. https://doi.org/10.1145/2601097.2601189

Akash Garg, Andrew O Sageman-Furnas, Bailin Deng, Yonghao Yue, Eitan Grinspun, Mark Pauly, and Max Wardetzky. 2014. Wire mesh design. *ACM Transactions on Graphics* 33, 4 (2014).

Ruslan Guseinov, Eder Miguel, and Bernd Bickel. 2017. CurveUps: Shaping Objects from Flat Plates with Tension-Actuated Curvature. *ACM Trans. Graph.* 36, 4, Article 64 (7 2017), 12 pages. https://doi.org/10.1145/3072959.3073709

Charles Hoberman. 1991. Radial expansion/retraction truss structures. US Patent 5,024,031.

David Jourdan, Melina Skouras, Etienne Vouga, and Adrien Bousseau. 2020. Printing-on-Fabric Meta-Material for Self-Shaping Architectural Models. In *Advances in Architectural Geometry*. http://www-sop.inria.fr/reves/Basilic/2020/JSVB20

Mina Konaković, Keenan Crane, Bailin Deng, Sofien Bouaziz, Daniel Piker, and Mark Pauly. 2016. Beyond developable: computational design and fabrication with auxetic materials. *ACM Transactions on Graphics (TOG)* 35, 4 (2016), 1–11.

Mina Konaković-Luković, Julian Panetta, Keenan Crane, and Mark Pauly. 2018. Rapid deployment of curved surfaces via programmable auxetics. *ACM Transactions on Graphics (TOG)* 37, 4 (2018), 106.

Julian Lienhard and Christoph Gengnagel. 2018. Recent developments in bending-active structures. In *Proceedings of IASS Annual Symposia*, Vol. 2018. International Association for Shell and Spatial Structures (IASS), 1–8.

Ligang Liu, Lei Zhang, Yin Xu, Craig Gotsman, and Steven J Gortler. 2008. A local/global approach to mesh parameterization. In *Computer Graphics Forum*, Vol. 27. Wiley Online Library, 1495–1504.

Luigi Malomo, Jesús Pérez, Emmanuel Iarussi, Nico Pietroni, Eder Miguel, Paolo Cignoni, and Bernd Bickel. 2018. FlexMaps: computational design of flat flexible shells for shaping 3D objects. *ACM Transactions on Graphics (TOG)* 37, 6 (2018), 1–14.

J Michael McCarthy and Gim Song Soh. 2010. *Geometric design of linkages*. Vol. 11. Springer Science & Business Media.

Robert McNeel et al. 2010. Rhinoceros 3D, Version 6.0. *Robert McNeel & Associates, Seattle, WA* (2010).

Giulio Molinari, Manfred Quack, Vitaly Dmitriev, Manfred Morari, Patrick Jenny, and Paolo Ermanni. 2011. Aero-structural optimization of morphing airfoils for adaptive wings. *Journal of Intelligent Material Systems and Structures* 22, 10 (2011), 1075–1089.

Julian Panetta, Florin Isvoranu, Tian Chen, Emmanuel Siéfert, Benoît Roman, and Mark Pauly. 2021. Computational inverse design of surface-based inflatables. *ACM Transactions on Graphics (TOG)* 40, 4 (2021), 1–14.

Julian Panetta, Mina Konaković-Luković, Florin Isvoranu, Etienne Bouleau, and Mark Pauly. 2019. X-Shells: A new class of deployable beam structures. *ACM Transactions on Graphics (TOG)* 38, 4 (2019), 1–15.

Julian Panetta, Abtin Rahimian, and Denis Zorin. 2017. Worst-Case Stress Relief for Microstructures. *ACM Trans. Graph.* 36, 4, Article 122 (jul 2017), 16 pages. https://doi.org/10.1145/3072959.3073649

Jesús Pérez, Miguel A Otaduy, and Bernhard Thomaszewski. 2017. Computational design and automated fabrication of kirchhoff-plateau surfaces. *ACM Transactions on Graphics (TOG)* 36, 4 (2017), 1–12.

Jesus Perez, Bernhard Thomaszewski, Stelian Coros, Bernd Bickel, José A. Canabal, Robert Sumner, and Miguel A. Otaduy. 2015. Design and Fabrication of Flexible Rod Meshes. *ACM Trans. on Graphics (Proc. of ACM SIGGRAPH)* 34, 4 (2015). http://www.gmrv.es/Publications/2015/PTCBCSO15

Stefan Pillwein, Kurt Leimer, Michael Birsak, and Przemyslaw Musialski. 2020. On Elastic Geodesic Grids and Their Planar to Spatial Deployment. *ACM Trans. Graph.* 39, 4, Article 125 (July 2020), 12 pages. https://doi.org/10.1145/3386569.3392490

Stefan Pillwein and Przemyslaw Musialski. 2021. Generalized Deployable Elastic Geodesic Grids. *arXiv preprint arXiv:2111.08883* (2021).

Christina L Randall, Evin Gultepe, and David H Gracias. 2012. Self-folding devices and materials for biomedical applications. *Trends in biotechnology* 30, 3 (2012), 138–146.

Yingying Ren, Julian Panetta, Tian Chen, Florin Isvoranu, Samuel Poincloux, Christopher Brandt, Alison Martin, and Mark Pauly. 2021. 3D weaving with curved ribbons. *ACM Transactions on Graphics (TOG)* 40, 4 (2021), 1–15.

Kelvin Roovers and Niels De Temmerman. 2017. Deployable scissor grids consisting of translational units. *International Journal of Solids and Structures* 121 (2017), 45–61.

Kelvin Roovers, Lara Alegria Mira, and Niels De Temmerman. 2013. From surface to scissor structure. In *Proceedings of the First Conference Transformables, Seville, Editorial Starbooks, Seville, Spain*, Vol. 2.

Andrew O Sageman-Furnas, Albert Chern, Mirela Ben-Chen, and Amir Vaxman. 2019. Chebyshev nets from commuting PolyVector fields. *ACM Transactions on Graphics (TOG)* 38, 6 (2019), 1–16.

Rohan Sawhney and Keenan Crane. 2017. Boundary first flattening. *ACM Transactions on Graphics (ToG)* 37, 1 (2017), 1–14.

Christian Schumacher, Jonas Zehnder, and Moritz Bächer. 2018. Set-in-Stone: Worst-Case Optimization of Structures Weak in Tension. *ACM Trans. Graph.* 37, 6, Article 252 (Dec. 2018), 13 pages. https://doi.org/10.1145/3272127.3275085

Mélina Skouras, Bernhard Thomaszewski, Bernd Bickel, and Markus Gross. 2012. Computational Design of Rubber Balloons. *Comput. Graphics Forum (Proc. Eurographics)* (2012).

Mélina Skouras, Bernhard Thomaszewski, Stelian Coros, Bernd Bickel, and Markus Gross. 2013. Computational Design of Actuated Deformable Characters. *ACM Trans. Graph.* 32, 4, Article 82 (jul 2013), 10 pages. https://doi.org/10.1145/2461912.2461979

Yichao Tang, Gaojian Lin, Shu Yang, Yun Kyu Yi, Randall D Kamien, and Jie Yin. 2017. Programmable Kiri-Kirigami Metamaterials. *Advanced Materials* 29, 10 (2017), 1604262.

Hideshi Tomita, Takashi Higaki, Toshiki Kobayashi, Takanari Fujii, and Kazuto Fujimoto. 2015. Stenting for curved lesions using a novel curved balloon: Preliminary experimental study. *Journal of Cardiology* 66, 2 (2015), 120–124. https://doi.org/10.1016/j.jjcc.2014.10.009

Ran Zhang, Thomas Auzinger, and Bernd Bickel. 2021. Computational Design of Planar Multistable Compliant Structures. *ACM Transactions on Graphics (TOG)* 40, 5 (2021), 1–16.

Ran Zhang, Shiwei Wang, Xuejin Chen, Chao Ding, Luo Jiang, Jie Zhou, and Ligang Liu. 2015. Designing planar deployable objects via scissor structures. *IEEE transactions on visualization and computer graphics* 22, 2 (2015), 1051–1062.

Xiaoting Zhang, Guoxin Fang, Melina Skouras, Gwenda Gieseler, Charlie C. L. Wang, and Emily Whiting. 2019. Computational Design of Fabric Formwork. *ACM Trans. Graph.* 38, 4, Article 109 (jul 2019), 13 pages. https://doi.org/10.1145/3306346.3322988

Changxi Zheng, Timothy Sun, and Xiang Chen. 2016. Deployable 3D linkages with collision avoidance.. In *Symposium on Computer Animation*. 179–188.